

# Elimination of the numerical Cerenkov instability for spectral EM-PIC codes

Peicheng Yu<sup>a</sup>, Xinlu Xu<sup>b</sup>, Viktor K. Decyk<sup>c</sup>, F. Fiuza<sup>d</sup>, Jorge Vieira<sup>e</sup>, Frank S. Tsung<sup>c</sup>, Ricardo A. Fonseca<sup>e,f</sup>, Wei Lu<sup>b</sup>, Luis O. Silva<sup>e</sup>, Warren B. Mori<sup>a,c</sup>

<sup>a</sup>*Department of Electrical Engineering, University of California Los Angeles, Los Angeles, CA 90095, USA*

<sup>b</sup>*Department of Engineering Physics, Tsinghua University, Beijing 100084, China*

<sup>c</sup>*Department of Physics and Astronomy, University of California Los Angeles, Los Angeles, CA 90095, USA*

<sup>d</sup>*Lawrence Livermore National Laboratory, Livermore, California, USA*

<sup>e</sup>*Instituto Superior Técnico, Lisbon, Portugal*

<sup>f</sup>*ISCTE - Instituto Universitário de Lisboa, 1649-026, Lisbon, Portugal*

---

## Abstract

When using an electromagnetic particle-in-cell (EM-PIC) code to simulate a relativistically drifting plasma, a violent numerical instability known as the numerical Cerenkov instability (NCI) occurs. The NCI is due to the unphysical coupling of electromagnetic waves on a grid to wave-particle resonances, including aliased resonances, i.e.,  $\omega + 2\pi\mu/\Delta t = (k_1 + 2\pi\nu_1/\Delta x_1)v_0$ , where  $\mu$  and  $\nu_1$  refer to the time and space aliases and the plasma is drifting relativistically at velocity  $v_0$  in the  $\hat{1}$ -direction. Recent studies have shown that an EM-PIC code which uses a spectral field solver and a low pass filter can eliminate the fastest growing modes of the NCI. Based on these studies a new spectral PIC code for studying laser wakefield acceleration (LWFA) in the Lorentz boosted frame was developed. However, we show that for parameters of relevance for LWFA simulations in the boosted frame, a relativistically drifting plasma is susceptible to a host of additional unstable modes with lower growth rates, and that these modes appear when the fastest growing unstable modes are filtered out. We show that these modes are most easily identified as the coupling between modes which are purely transverse (EM) and purely longitudinal (Langmuir) in the rest frame of the plasma for specific time and space aliases. We rewrite the dispersion

---

*Email address:* xux110@mails.tsinghua.edu.cn (Xinlu Xu)

relation of the drifting plasma for a general field solver and obtain analytic expressions for the location and growth rate for each unstable mode, i.e, for each time and space aliased resonances. We show for the spectral solver that when the fastest growing mode is eliminated a new mode at the fundamental resonance ( $\mu = \nu_1 = 0$ ) can be seen. This mode is highly localized in  $\mathbf{k}$ -space to four dots in two dimensions and rings in three dimensions, and for time steps near the Courant limit its growth rate is usually one order of magnitude smaller than that of the fastest growing mode at the first spatial aliasing ( $\nu_1 = \pm 1$ ) of the Langmuir modes. This is different than the Yee solver for which the NCI growth rate at the fundamental Langmuir mode and at the first spatial aliasing Langmuir mode are of the same order of magnitude. It is also found that in LWFA simulation in the Lorentz boosted frame using a spectral EM-PIC code, the NCI within the fundamental zone ( $\mu = \nu_1 = 0$ ) occurs for wave numbers that lie within the range of modes that are physically important for time steps near the Courant limit. These modes can also be eliminated through appropriate masks in  $\mathbf{k}$ -space. However, unlike the fastest growing modes, these new modes can also be eliminated by reducing the time step. Meanwhile, as the time step is reduced, these new modes move to higher wave numbers outside the physically important range and their growth rate decreases. It is further shown that near the Courant limit the growth rate of the third fastest growing NCI modes in the spectral solver can be reduced by using higher order particle shapes. As the time step is reduced the growth rates of higher order modes, which are due to the coupling of higher order wave-particle resonance, are reduced as well. Based on these conclusions, we can effectively eliminate the NCI when using the spectral solver. The fastest growing modes are eliminated by a dedicated low-pass filter. The second fastest growing modes can be eliminated through the use of a  $\mathbf{k}$ -space mask and/or reducing the time step which moves the modes to  $\mathbf{k}$  outside the interesting physics and reduces their growth rate. The growth rate of the third fastest growing modes are reduced by using higher order particle shapes and/or reducing the time step. Importantly, unlike when using a finite difference based algorithm, the accuracy improves with reduced time step so any result can be compared against cases with very small time steps. Examples of both laser wakefield acceleration in the boosted frames and relativistic collisionless shocks are presented. The results show that high fidelity multi-dimensional simulations of drifting plasmas can be carried out with a spectral EM solver with no evidence of numerical Cerenkov instability.

*Keywords:* Particle-in-cell, plasma simulation, relativistic drifting plasma, numerical Cerenkov instability, numerical dispersion relation, spectral solver

---

## 1. Introduction

The study of the multi-dimensional numerical Cerenkov instability (NCI) in electromagnetic particle-in-cell (EM-PIC) plasma simulations has attracted much renewed attention since the identification of this numerical instability as the limiting factor [10, 11, 12] of Lorentz boosted frame simulations for laser wakefield acceleration (LWFA) [1, 2, 3, 4]. Furthermore, the NCI is also a limiting factor in relativistic collisionless shock simulations [5, 6]. Early and recent work has shown that the NCI inevitably arises in EM-PIC simulations when a plasma (neutral or pure electron) drifts across a simulation grid with a speed near the speed of light. Analysis shows that it is due to the unphysical coupling of electromagnetic like modes and wave particle resonances (including those due to aliasing) [7, 8, 10, 11, 12]. This instability leads to unphysical exponential growth of the EM field energy which interferes with the physics being studied in the simulation. As a result, significant recent effort has been devoted to the understanding and elimination of the NCI so that high fidelity relativistic plasma drift simulations can be routinely performed [7, 8, 9, 10, 11, 12, 13, 14, 15].

In this recent work, dispersion relations for the NCI has been derived and analyzed. We begin by restating the dispersion tensor provided in Ref. [12]. This tensor can be used to study the pattern and growth rates of the NCI in Fourier space. For a cold plasma drifting in  $\hat{1}$ -direction relativistically with the unperturbed normalized distribution function of

$$f_0^n = \delta(p_1 - p_0)\delta(p_2)\delta(p_3) \quad (1)$$

where  $p_0 = \gamma v_0$ , and  $v_0$  is the drifting velocity of the plasma, the corresponding dispersion relation for the plasma drift is [12]

$$\text{Det}(\overleftarrow{\epsilon}) = 0 \quad (2)$$

where the elements of  $\overleftrightarrow{\epsilon}$  are

$$\begin{aligned}
\epsilon_{11} &= [\omega]^2 - [k]_{E2}[k]_{B2} - [k]_{E3}[k]_{B3} \\
&\quad - \frac{\omega_p^2}{\gamma} \sum_{\mu,\nu} (-1)^\mu \frac{S_{j1} \{ S_{E1}[\omega] \omega' / \gamma^2 + v_0^2 (S_{B3} k'_2 [k]_{E2} + S_{B2} k'_3 [k]_{E3}) \}}{(\omega' - k'_1 v_0)^2} \\
\epsilon_{12} &= [k]_{E1}[k]_{B2} - \frac{\omega_p^2}{\gamma} \sum_{\mu,\nu} (-1)^\mu \frac{S_{j1} v_0 k'_2 (S_{E2}[\omega] - v_0 S_{B3}[k]_{E1})}{(\omega' - k'_1 v_0)^2} \\
\epsilon_{13} &= [k]_{E1}[k]_{B3} - \frac{\omega_p^2}{\gamma} \sum_{\mu,\nu} (-1)^\mu \frac{S_{j1} v_0 k'_3 (S_{E3}[\omega] - v_0 S_{B2}[k]_{E1})}{(\omega' - k'_1 v_0)^2} \\
\epsilon_{21} &= [k]_{E2}[k]_{B1} - \frac{\omega_p^2}{\gamma} \sum_{\mu,\nu} (-1)^\mu \frac{v_0 S_{j2} S_{B3}[k]_{E2}}{\omega' - k'_1 v_0} \\
\epsilon_{22} &= [\omega]^2 - [k]_{E1}[k]_{B1} - [k]_{E3}[k]_{B3} - \frac{\omega_p^2}{\gamma} \sum_{\mu,\nu} (-1)^\mu \frac{S_{j2} (S_{E2}[\omega] - v_0 S_{B3}[k]_{E1})}{\omega' - k'_1 v_0} \\
\epsilon_{23} &= [k]_{E2}[k]_{B3} \\
\epsilon_{31} &= [k]_{E3}[k]_{B1} - \frac{\omega_p^2}{\gamma} \sum_{\mu,\nu} (-1)^\mu \frac{v_0 S_{j3} S_{B2}[k]_{E3}}{\omega' - k'_1 v_0} \\
\epsilon_{32} &= [k]_{E3}[k]_{B2} \\
\epsilon_{33} &= [\omega]^2 - [k]_{E1}[k]_{B1} - [k]_{E2}[k]_{B2} - \frac{\omega_p^2}{\gamma} \sum_{\mu,\nu} (-1)^\mu \frac{S_{j3} (S_{E3}[\omega] - v_0 S_{B2}[k]_{E1})}{\omega' - k'_1 v_0}
\end{aligned} \tag{3}$$

where  $[\omega]$ ,  $[k]_{E,B}$  are the finite difference operators of the Maxwell Equation solver,  $\mathbf{S}_j$ ,  $\mathbf{S}_E$  and  $\mathbf{S}_B$  are the current and field interpolation functions (the definitions for  $[\omega]$ ,  $[k]_{E,B}$ ,  $\mathbf{S}_j$ ,  $\mathbf{S}_E$ , and  $\mathbf{S}_B$  for each Maxwell solver are given in the Appendix of Ref. [12]).  $v_0$  is normalized by the speed of light.  $\omega_p$  is the plasma frequency with

$$\omega_p^2 = \frac{4\pi q^2 n_0}{m} \tag{4}$$

where  $q$  and  $m$  are the electron charge and rest mass,  $n_0$  the plasma density,

and

$$\begin{aligned} \omega' &= \omega + \mu\omega_g & \omega_g &= \frac{2\pi}{\Delta t} & \mu &= 0, \pm 1, \pm 2, \dots \\ k'_i &= k_i + \nu_i k_{gi} & k_{gi} &= \frac{2\pi}{\Delta x_i} & \nu_i &= 0, \pm 1, \pm 2, \dots \end{aligned} \quad (5)$$

Due to the use of finite space and time steps, these dispersion relations not only contain terms from the lowest order Brillouin zones ( $\mu = 0$  and  $\boldsymbol{\nu} = \mathbf{0}$ ), but also the space aliasing (summation over  $\boldsymbol{\nu}$ ) and time aliasing (summation over  $\mu$ ) terms [16, 17]. The elements of the interpolation functions  $\mathbf{S}_{j,E,B}$ , and finite difference operators  $[\cdot]$  vary depending on the field solver (e.g., spectral [18, 19], Yee [20], or Karkkainen solver [21]), particle shape, current deposition algorithm, and field interpolation (e.g., momentum or field conserving).

The NCI modes can be found by solving Eq. (2) numerically or analytically by specifying a  $\mu$  and  $\boldsymbol{\nu}$  [12]. The unstable modes are found near the intersections of the beam resonances ( $\omega' - k'_1 v_0 = 0$ ), and the EM modes ( $[\omega]^2 = [k]^2$  in vacuum). Since the numerical dispersion relation of the EM modes is mainly determined by the Maxwell field solver used in the simulation, the location of the unstable NCI modes can be manipulated through the choice of the Maxwell solver. For example, in [12] it was shown that using a spectral Maxwell solver, i.e., solving Maxwell's equations in  $\mathbf{k}$ -space [18, 19], moves the fastest growing modes to a region in  $\mathbf{k}$ -space far away from the modes of physical interest. In this case, the fastest growing modes all come from the first spatial aliasing beam ( $\mu = 0, \nu_1 = \pm 1$ ) resonance. For a Yee solver, the fast growing modes come from this resonance, as well as from the fundamental mode ( $\mu = \nu_1 = 0$ ) which leads to growth at  $\mathbf{k}$  that resides in the middle of the interesting physics. In [12] it was shown that the fastest growing NCI mode for a spectral solver could be eliminated by applying a low pass filter in the solver.

Based on these results the feasibility of using an EM-PIC code with spectral solver to eliminate the NCI for LWFA simulations in a Lorentz boosted frame was subsequently investigated in [13]. For weakly nonlinear laser drivers the agreement between the rest and Lorentz boosted frames was excellent for arbitrary  $\gamma$ . For nonlinear cases, the lineouts of the wakefield in Fig. 8 in Ref. [13] showed differences at the highest  $\gamma$ . Based on these differences, in this paper we have examined further both the growth rates and methods for eliminating lower growing NCI unstable modes with an emphasis

for the spectral solver. We note that Godfrey and co-workers have proposed methods to reduce the growth rate of the NCI for finite difference solvers [15]. They have also discussed the NCI characters of an FFT based analytical time domain solver and concentrate on time steps larger than the Courant limit of the spectral Maxwell solver [14]. The work presented here can be viewed as complimentary since there are advantages and disadvantages for each type of solver and for using large or small time steps.

To systematically investigate these additional unstable modes, we rewrite the numerical dispersion relation into the form of two coupled modes whose coupling term vanishes in the continuous limit with  $\Delta t \rightarrow 0$  and  $\Delta x_i \rightarrow 0$ . These two coupled modes can be identified as the numerical form of the Lorentz transformation of modes which are purely longitudinal (plasma oscillations) and purely transverse (EM waves) in the rest frame of the plasma. These modes are uncoupled in the rest frame in the continuous limit. Therefore, in the continuous limit where Lorentz invariance is strictly true they are also decoupled, although no longer remaining purely longitudinal and transverse. However, we show that in the discrete limit there is a non-vanishing coupling term in the dispersion relation. The coupling term explicitly shows how the finite grid and time step leads to the inevitable coupling between these modes which leads to instability.

Recasting the dispersion relation in this new form not only sheds light on the mechanism of the NCI, but also provides a natural way of systematically calculating the unstable NCI modes. We use this dispersion relation to obtain analytical expressions for the family of unstable modes which includes the dependence of growth rate on the grid size, time step, and plasma density; as well as the location of the modes in  $\mathbf{k}$ -space. We find excellent agreement between the analytical expressions, numerical solutions to the dispersion relation, and PIC simulations.

Based on these new results, we have experimented with different strategies for eliminating the first, second, and higher order unstable NCI modes with an emphasis for the spectral solver. As has been demonstrated in [12, 13], when a low pass filter is used the fastest growing NCI modes [at  $(\mu, \nu_1) = (0, \pm 1)$ ] are completely eliminated in the spectral solver. In addition, we find that for the parameter space of interest the second fastest growing modes are those at  $(\mu, \nu_1) = (0, 0)$ . These modes have a highly localized pattern of four dots in Fourier space (one in each quadrant) in 2D and two rings in 3D. Since in some cases the unstable modes can reside near or in the middle of modes of physical interest, filtering them out directly could potentially affect

the accuracy of the physics model. However, we find that unlike the fastest growing modes, the location and growth rate of these  $(\mu, \nu_1) = (0, 0)$  mode depend on the time step as well as the plasma density. As the time step is reduced these modes move to higher values of wave number well outside the region of physical interest and their growth rate is greatly reduced. Thus, these modes can be eliminated by reducing the time step, and/or using a filter if they do not overlap with the physical modes. We also find that the location, growth rate, and the values of  $(\mu, \nu_1)$  of the next fastest growing modes depend on the time step and particle shape, and reducing the time step can also effectively eliminate these modes as well. These results reveal one clear advantage of spectral EM-PIC codes: the results always converge as the time step is reduced, which allows one to check the validity of any simulation.

We then present results from LWFA simulations in the nonlinear regime using this new understanding of the location and growth rate of the unstable modes. We have performed simulations of LWFA in a nonlinear regime, with time steps near the Courant limit with a low pass filter to eliminate the fastest growing mode, with a mask to eliminate the second fastest growing mode, and with second order particle shapes to eliminate the third fastest growing modes. We have also repeated these simulations where we use a low pass filter and reduce the time step to 1/8 of the Courant limit with no mask. For the later case, excellent agreement with the lab frame results at the highest  $\gamma$  is observed. In the last section, we summarize the results and discuss areas for future work.

## 2. Spectral solver NCI mode in 2D

Without loss of generality, we systematically investigate the NCI modes by starting from the numerical dispersion relation of a 2D drifting plasma

with the appropriate elements of the dispersion tensor  $\overleftrightarrow{\epsilon}$  [12]

$$\begin{aligned}
\epsilon_{11} &= [\omega]^2 - [k]_{E2}[k]_{B2} - \frac{\omega_p^2}{\gamma} \sum_{\mu, \nu} (-1)^\mu \frac{S_{j1}(S_{E1}\omega'/\gamma^2 + S_{B3}[k]_{E2}k_2'v_0^2)}{(\omega' - k_1'v_0)^2} \\
\epsilon_{12} &= [k]_{E1}[k]_{B2} - \frac{\omega_p^2}{\gamma} \sum_{\mu, \nu} (-1)^\mu \frac{k_2'v_0 S_{j1}(S_{E2}[\omega] - S_{B3}v_0[k]_{E1})}{(\omega' - k_1'v_0)^2} \\
\epsilon_{21} &= [k]_{E2}[k]_{B1} - \frac{\omega_p^2}{\gamma} \sum_{\mu, \nu} (-1)^\mu \frac{S_{j2}S_{B3}[k]_{E2}v_0}{\omega' - k_1'v_0} \\
\epsilon_{22} &= [\omega]^2 - [k]_{E1}[k]_{B1} - \frac{\omega_p^2}{\gamma} \sum_{\mu, \nu} (-1)^\mu \frac{S_{j2}(S_{E2}[\omega] - S_{B3}[k]_{E1}v_0)}{\omega' - k_1'v_0} \\
\epsilon_{33} &= [\omega]^2 - [k]_{E1}[k]_{B1} - [k]_{E2}[k]_{B2} - \frac{\omega_p^2}{\gamma} \sum_{\mu, \nu} (-1)^\mu \frac{S_{j3}(S_{E3}[\omega] - S_{B2}[k]_{E1}v_0)}{\omega' - k_1'v_0} \\
\epsilon_{13} &= \epsilon_{23} = \epsilon_{31} = \epsilon_{32} = 0
\end{aligned} \tag{6}$$

We focus on the  $\mathbf{k}$  near the beam resonance line [12]

$$\omega' - k_1'v_0 = 0. \tag{7}$$

The numerical solution of Eq. (2) for each mode can be analytically obtained by keeping only the corresponding  $\mu$  and  $\nu$  terms in Eq. (6) since these terms are dominant near the corresponding resonance lines. Note for the cases considered in this paper, we find it is a good approximation to truncate the sum of  $\nu_2$  and only keep the  $\nu_2 = 0$  term. The corresponding dispersion relation  $\epsilon_{11}\epsilon_{22} - \epsilon_{12}\epsilon_{21} = 0$  becomes

$$\begin{aligned}
&\left( [\omega]^2 - [k]_{E2}[k]_{B2} - \frac{\omega_p^2}{\gamma} (-1)^\mu \frac{S_{j1}(S_{E1}[\omega]\omega'/\gamma^2 + S_{B3}v_0^2[k]_{E2}k_2')}{(\omega' - k_1'v_0)^2} \right) \times \\
&\left( [\omega]^2 - [k]_{E1}[k]_{B1} - \frac{\omega_p^2}{\gamma} (-1)^\mu \frac{S_{j2}(S_{E2}[\omega] - S_{B3}[k]_{E1}v_0)}{\omega' - k_1'v_0} \right) - \\
&\left( [k]_{E1}[k]_{B2} - \frac{\omega_p^2}{\gamma} (-1)^\mu \frac{S_{j1}v_0k_2'(S_{E2}[\omega] - S_{B3}[k]_{E1}v_0)}{(\omega' - k_1'v_0)^2} \right) \times \\
&\left( [k]_{E2}[k]_{B1} - \frac{\omega_p^2}{\gamma} (-1)^\mu \frac{S_{j2}S_{B3}v_0[k]_{E2}}{\omega' - k_1'v_0} \right) = 0
\end{aligned} \tag{8}$$



After some algebra, Eq. (8) can be written as

$$\begin{aligned} & \left( (\omega' - k'_1 v_0)^2 - \frac{\omega_p^2}{\gamma^3} (-1)^\mu \frac{S_{j1} S_{E1} \omega'}{[\omega]} \right) \times \\ & \left( [\omega]^2 - [k]_{E1} [k]_{B1} - [k]_{E2} [k]_{B2} - \frac{\omega_p^2}{\gamma} (-1)^\mu \frac{S_{j2} (S_{E2}[\omega] - S_{B3} [k]_{E1} v_0)}{\omega' - k'_1 v_0} \right) \\ & + \mathcal{C} = 0 \end{aligned} \quad (9)$$

where  $\mathcal{C}$  is a coupling term in the dispersion relation

$$\begin{aligned} \mathcal{C} = \frac{\omega_p^2}{\gamma} \frac{(-1)^\mu}{[\omega]} \left\{ S_{j1} S_{E1} \omega' [k]_{E2} [k]_{B2} (v_0^2 - 1) + S_{j2} S_{E2} [k]_{E2} [k]_{B2} (\omega' - k'_1 v_0) \right. \\ \left. + S_{j1} [k]_{E2} (S_{E2} [k]_{B1} k_2 v_0 - S_{B3} k_2 v_0^2 [\omega]) \right\} \end{aligned} \quad (10)$$

Much can be learned by investigating Eq. (9). First, in the continuous limit ( $\Delta t \rightarrow 0$ ,  $\Delta x_i \rightarrow 0$ , and  $\nu_1 = 0$ ), we have  $[\omega] \rightarrow \omega$ ,  $S_{E,B} \rightarrow 1$ , so the coupling term  $\mathcal{C}$  vanishes; second, the first two terms of Eq. (9) are the Lorentz transformation of the dispersion relation of the Langmuir (longitudinal) mode, and the EM (transverse) mode in a stationary plasma, which in the continuous limit reduce to

$$(\omega - k_1 v_0)^2 - \frac{\omega_p^2}{\gamma^3} = 0 \quad \omega^2 - k_1^2 - k_2^2 - \frac{\omega_p^2}{\gamma} = 0 \quad (11)$$

Consequently, we can identify the numerical Langmuir modes and EM modes for a drifting plasma as

$$(\omega' - k'_1 v_0)^2 - \frac{\omega_p^2}{\gamma^3} (-1)^\mu \frac{S_{j1} S_{E1} \omega'}{[\omega]} \approx 0 \quad (12)$$

$$[\omega]^2 - [k]_{E1} [k]_{B1} - [k]_{E2} [k]_{B2} - \frac{\omega_p^2}{\gamma} (-1)^\mu \frac{S_{j2} (S_{E2}[\omega] - S_{B3} [k]_{E1} v_0)}{\omega' - k'_1 v_0} \approx 0 \quad (13)$$

In addition, from Eq. (9) we see that when finite grid sizes and time steps are used neither Eq. (12) nor Eq. (13) leads to instability (if the Courant limit is satisfied). Therefore it becomes clear that the NCI is caused by the numerical coupling between modes which are purely longitudinal and purely transverse in the plasma rest frame due to the non-vanishing term  $\mathcal{C}$ . In [12] the conclusion that NCI can be found near the intersections of the EM modes

and Langmuir modes (or equivalently  $\omega' - k'_1 v_0 = 0$  since the  $\omega_p^2/\gamma^3$  term is negligible) is obtained from examining the simulation and numerical data. With the new form Eq. (9), we can now directly see how the Langmuir mode couples to the EM modes. Therefore, reducing or eliminating the coupling term  $\mathcal{C}$  is the key to mitigating the NCI. Another interesting fact obtained from Eq. (9) is that, if we assume that the  $\omega_p^2$  term in Eq. (12) and (13) are small and can be neglected, when determining the positions of these two modes in Fourier space, the time and space aliasing  $\mu$  and  $\nu_1$  are in the Langmuir modes, while there is no aliasing part in the EM mode. As a side note, it is evident from Eq. (19) of [12] that in 1D the coupling term vanishes,  $\mathcal{C} = 0$ , in the numerical dispersion relation, hence no NCI is found in 1D.

For each pair of  $(\mu, \nu_1)$  there is a corresponding Eq. (9). However, in PIC algorithm the range of  $(\omega, k_1)$  for the quantities defined at discrete locations and time step is limited to the fundamental Brillouin zone  $k_i \in (-k_{gi}/2, k_{gi}/2)$ ,  $\omega \in (-\omega_g/2, \omega_g/2)$ . As a result, not all the  $(\mu, \nu_1)$  wave-particle resonance line exist within the fundamental Brillouin zone. In the following, we describe a way to systematically identify the wave-particle resonance lines inside the fundamental zone. Take the parameters in Table 1 as an example, we first plot the  $(\mu, \nu_1) = (0, 0)$  line [blue line in Fig. 1]. As the line extends to the right it meets the boundary of the fundamental zone at  $k_1 = 0.5k_{g1}$ . To further extend it into the fundamental zone we add  $\nu_1$  by 1, fold the line to the right boundary of  $k_1$ , and obtain the  $(\mu, \nu_1) = (0, 1)$  line [red line in Fig. 1]. The red line extends further until it reaches the  $\omega = 0.5\omega_g$  boundary. To extend it further we increase  $\mu$  by 1, and obtain the  $(\mu, \nu_1) = (1, 1)$  line. More higher order modes in the fundamental Brillouin zone can be obtained in this way. The negative  $(\mu, \nu_1)$  lines can likewise be obtained by starting from the main Langmuir mode and then extending it to the left, and sets of these  $(\mu, \nu_1)$  lines can be obtained as the lines hit the boundary at  $\omega = -0.5\omega_g$  ( $\mu$  is reduced by 1) and  $k_1 = -0.5k_{g1}$  ( $\nu_1$  is reduced by 1). Using the normalization

$$\hat{\omega} + \mu = v_0(\hat{k}_1 + \nu_1)\lambda_1 \quad (14)$$

where

$$\hat{\omega} = \frac{\omega}{\omega_g} \quad \hat{k}_i = \frac{k_i}{k_{gi}} \quad \lambda_i = \frac{\Delta t}{\Delta x_i} \quad (15)$$

the criterion for the Langmuir modes to be inside the fundamental Brillouin zone are  $|v_0\lambda_1\nu_1 - \mu| < 0.5 + 0.5v_0\lambda_1$ . We can see that when  $\lambda_1 > 1$  for each  $\mu$

there is only one  $\nu_1$  in the fundamental zone; while for  $\lambda_1 < 1$  for each  $\nu_1$  there is only one  $\mu$  that satisfies this condition. Note for explicit Maxwell solvers  $\lambda_1 < 1$  is a requirement for stable propagation of EM waves in vacuum. The NCI occurs where a resonance line intersects the EM dispersion relation. In Fig. 1 we also plot the EM dispersion relation in vacuum as dashed lines. Note for EM curves we only show  $\hat{\omega}$  v.s.  $\hat{k}_1$  at  $\hat{k}_2 = 0$ , but this line varies as  $\hat{k}_2$  changes. For the NCI pattern and growth rates associated with each resonance line, we can numerically solve Eq. (9) using the corresponding  $\mu$  and  $\nu_1$ . Note in [11] a plot similar to Fig. 1 can be found (Fig. 1 of Ref. [11]). However, in [11] all the  $\mu$  are summed over analytically, while in this paper we emphasize that for a particular resonance line, only one  $\mu$  term in the elements of  $\overleftrightarrow{\epsilon}$  is playing a dominant role. Furthermore, care should be taken when summing over  $\mu$  and  $\nu_1$  as they are not independent sums.

While Eq. (9) can be used to study the fastest growing mode at  $(\mu, \nu_1) = (0, \pm 1)$  which was investigated in Ref. [12] and [13], here we concentrate on the additional modes. We use Eq. (9) to develop analytical expressions within the parameter space we are interested in. Starting from Eq. (9), we expand  $\omega'$  around the beam resonance  $\omega' = k'_1 v_0$ , and write  $\omega' = k'_1 v_0 + \delta\omega$ , where  $\delta\omega$  is a small term. In addition, we use the relativistic limit  $v_0 \rightarrow 1$ , and expand the finite difference operator  $[\omega]$  as

$$[\omega] \approx [k'_1 v_0] + \delta\omega \left. \frac{\partial[\omega]}{\partial\omega} \right|_{k'_1 v_0} \quad [\omega]^2 \approx [k'_1 v_0]^2 + 2[k'_1 v_0] \delta\omega \left. \frac{\partial[\omega]}{\partial\omega} \right|_{k'_1 v_0} \quad (16)$$

where

$$[k'_1 v_0] \equiv \xi_0 = \frac{\sin(k'_1 \Delta t / 2)}{\Delta t / 2} \quad \left. \frac{\partial[\omega]}{\partial\omega} \right|_{k'_1 v_0} \equiv \xi_1 = \cos(k'_1 \Delta t / 2) \quad (17)$$

In addition, we found it is sufficiently accurate if we neglect the  $\omega^2/\gamma^3$  term in the Langmuir mode in Eq. (9). This is why it is essentially the same to say that the instability occurs at wave-particle resonances, beam resonances, or at Langmuir resonances. Using these approximations, we obtain a cubic equation for  $\delta\omega$ ,

$$A_1 \delta\omega^3 + A_2 \delta\omega^2 + A_3 \delta\omega + A_4 = 0 \quad (18)$$

where

$$\begin{aligned}
A_1 &= 2\xi_0\xi_1k'_1 \\
A_2 &= k'_1 \left\{ \xi_0^2 - [k]_{E1}[k]_{B1} - [k]_{E2}[k]_{B2} - \frac{\omega_p^2}{\gamma}(-1)^\mu S_{j2}S_{E2}\xi_1 \right\} \\
A_3 &= \frac{\omega_p^2}{\gamma}(-1)^\mu \left\{ k'_1 S_{j2}(S_{B3}[k]_{E1} - S_{E2}\xi_0) + S_{j1}[k]_{E2}(S_{E2}[k]_{B2} - S_{B3}k_2\xi_1) \right\} \\
A_4 &= \frac{\omega_p^2}{\gamma}(-1)^\mu [k]_{E2}k_2 S_{j1} \left( S_{E2}[k]_{B1} - S_{B3}\xi_0 \right) \tag{19}
\end{aligned}$$

If we further assume  $\cos(\omega\Delta t/2) \approx \cos(k'_1\Delta t/2)$  (this term appears in  $S_{Bi}$ , see Appendix of [12]), the coefficients  $A_1$  to  $A_4$  are real, and completely determined by  $k_1$  and  $k_2$ . When the discriminant of this cubic equation

$$\Delta = 18A_1A_3A_3A_4 - 4A_2^3A_4 + A_2^2A_3^2 - 4A_1A_3 - 27A_1^2A_4^2 \tag{20}$$

satisfies the condition  $\Delta < 0$ , the cubic equation has one real root and two non-real complex conjugate roots. Therefore, by calculating the discriminant of the cubic equation Eq. (20), we can quickly identify the position of the instability for a particular  $\nu_1$ . We can then use the general formula for the roots of a cubic equation to obtain the growth rate of the corresponding  $\mathbf{k}$  mode. As a result, by solving Eq. (18) and (19) we can rapidly calculate the location and growth rate of the instability.

Up until now, the derivation can be applied to any Maxwell solver. We now concentrate on the spectral solver which is the main focus of this paper. For this case  $[\mathbf{k}]_{E,B} = \mathbf{k}$ , and

$$S_{E1} = S_{E2} = S_{E3} \equiv S_E = S_l \quad S_{B1} = S_{B2} = S_{B3} \equiv S_B = \cos \frac{\omega\Delta t}{2} S_l.$$

where

$$S_l = \left( \frac{\sin(k_1\Delta x_1/2)}{k_1\Delta x_1/2} \right)^{l+1} \left( \frac{\sin(k_2\Delta x_2/2)}{k_1\Delta x_2/2} \right)^{l+1} \tag{21}$$

and  $l$  corresponds to the order of the particle shape. Eq. (9) reduces to

$$\begin{aligned}
&\left( (\omega' - k'_1 v_0)^2 - \frac{\omega_p^2}{\gamma^3}(-1)^\mu \frac{S_j S_E \omega'}{[\omega]} \right) \left( [\omega]^2 - k_1^2 - k_2^2 - \frac{\omega_p^2}{\gamma}(-1)^\mu S_j \frac{S_E[\omega] - S_B k_1 v_0}{\omega' - k'_1 v_0} \right) \\
&+ \frac{\omega_p^2}{\gamma[\omega]}(-1)^\mu S_j k_2^2 \{ v_0^2 (S_E \omega - S_B[\omega]) - v_0 \nu_1 S_E k_{g1} \} = 0 \tag{22}
\end{aligned}$$

and the corresponding coefficients  $A_1$  to  $A_4$  are

$$\begin{aligned}
A_1 &= 2\xi_0\xi_1k'_1 \\
A_2 &= k'_1(\xi_0^2 - \frac{\omega_p^2}{\gamma}S_jS_E\xi_1 - k_1^2 - k_2^2) \\
A_3 &= \frac{\omega_p^2}{\gamma}S_j(S_Bk_1k'_1 - S_E\xi_0k'_1 + S_Ek_2^2 - S_Bk_2^2\xi_1) \\
A_4 &= \frac{\omega_p^2}{\gamma}S_jk_2^2(S_Ek_1 - S_B\xi_0)
\end{aligned} \tag{23}$$

As stated above we use the approximation  $\cos(\omega\Delta t/2) \approx \cos(k'_1\Delta t/2)$  when solving the cubic equation, and  $A_1$  to  $A_4$  are real, and completely determined by  $k_1$  and  $k_2$ .

Following the prescription described above for each  $(\mu, \nu_1)$  modes, we systematically investigate the NCI modes for the spectral solver. In Fig. 2 (b), (d), and (f) we present the three sets of modes with the highest growth rate calculated by the analytical expressions Eqs. (18) and (23), for the parameters listed in Table 1, and for linear particle shapes ( $l = 1$ ). Fig. 2 (b) shows the modes with  $(\mu, \nu_1) = (0, \pm 1)$ , which are the fastest growing NCI modes. These modes were already studied in [12]. Fig. 2 (d) shows the  $(\mu, \nu_1) = (0, 0)$  modes, which have a highly localized pattern of four dots [note that in (d) only one quadrant is plotted]. These modes usually have a maximum growth rate one order of magnitude smaller than the  $(\mu, \nu_1) = (0, \pm 1)$  modes. For the parameters listed in Table 1, the next fastest growing modes are the  $(\mu, \nu_1) = (\pm 1, \pm 2)$  modes which have a maximum growth rate approximately 3 times smaller than the  $(\mu, \nu_1) = (0, 0)$  modes (for linear particle shape).

We have similarly performed UPIC-EMMA simulations in 2D to observe various NCI modes in the spectral solver, and to compare with the theory presented above. The simulations use a neutral plasma drifting at relativistic velocity, with the Lorentz factor  $\gamma = 50.0$ . The plasma has a uniform initial spatial distribution, and we used the parameters listed in Table 1. Note these parameters are those commonly used in the LWFA simulation in the Lorentz boosted frame [13], and the plasma density is 100 times larger than that used in [12].

Fig. 2 (a), (c), and (e) show the simulation data of the FFT of  $E_2$  at a particular time during the exponential EM energy growth from the NCI [12]. Fig. 2 (a) shows results from a simulation with no low-pass filter, and the

Parameters	Values
grid size $(k_p\Delta x_1, k_p\Delta x_2)$	$(0.2, 0.2)$
time step $\Delta t$	$0.4\Delta x_1$
boundary condition	Periodic
simulation box size $(L_1, L_2)$	$102.4 \times 102.4$
plasma drifting Lorentz factor	$\gamma = 50.0$
plasma density	$n/n_p = 100.0$

Table 1: Crucial simulation parameters for the 2D relativistic plasma drift simulation.  $n_p$  is the reference plasma density, and  $\omega_p^2 = 4\pi q^2 n_p/m_e$ ,  $k_p = \omega_p$  ( $c$  is normalized to 1).

most prominent modes are the  $(\mu, \nu_1) = (0, \pm 1)$  modes that were analyzed in detail in Ref. [12]. To generate the frames in the middle row, we use a low-pass filter to eliminate the  $(\mu, \nu_1) = (0, \pm 1)$  modes. This makes the unstable  $(\mu, \nu_1) = (0, 0)$  modes more noticeable. It is shown in Fig. 2 (c) that the  $(\mu, \nu_1) = (0, 0)$  modes have a highly localized pattern of four dots [in Fig. 2 only one quadrant is shown], which agrees with the prediction of the analytic expression. According to Fig. 1, there is no intersection between  $(\mu, \nu_1) = (1, 1)$  resonance [and  $(\mu, \nu_1) = (-1, -1)$  resonance] and the EM dispersion relation, so the next set of modes of interest are the  $(\mu, \nu_1) = (1, 2)$  and  $(\mu, \nu_1) = (-1, -2)$  modes. To make the  $(\mu, \nu_1) = (\pm 1, \pm 2)$  mode more noticeable, we use a low-pass filter to filter out the  $(\mu, \nu_1) = (0, \pm 1)$  mode, plus a four-dot mask filter to remove the  $(\mu, \nu_1) = (0, 0)$  mode. As shown in Figs. 2 (e) and (f), the locations of these modes in the simulation agree with the analytic prediction. As a side note, this numerical experiment also shows the simplicity and flexibility of using filters (masks) with complicated shapes in a spectral EM-PIC code to control the unphysical NCI growth.

According to both the theory and simulations, in the parameter space we are interested in, we usually categorize the NCI for a spectral solver into three categories: the fastest growing modes at  $(\mu, \nu_1) = (0, \pm 1)$ ; the second fastest growing modes at  $(\mu, \nu_1) = (0, 0)$ ; and higher order NCI modes with  $|\nu_1| > 1$  that have an even smaller growth rate. In the following we will discuss how the locations and positions of these modes change with the simulation parameters.

For the NCI modes with  $|\nu_1| \geq 1$ , the instability resides around the intersections of the Langmuir mode and EM mode [12, 13]:

$$(1 - v_0^2)k_1^2 + k_2^2 - 2\beta\xi k_1 - \xi^2 = 0 \quad (24)$$

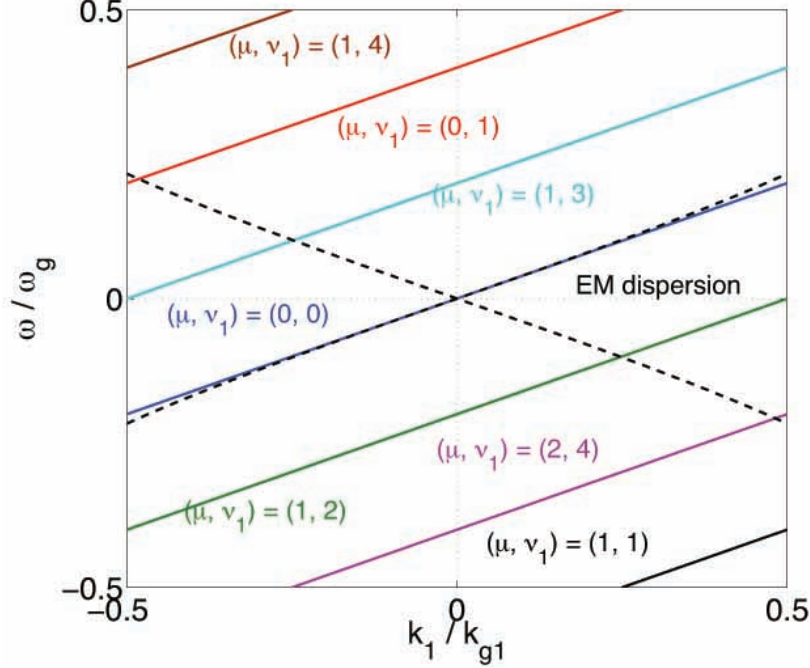


Figure 1: The EM dispersion relation together with the beam resonance  $\omega' - k_1'\beta = 0$  is shown. The parameters used to plot this figure are listed in Table 1.

where  $\xi = \beta\nu_1 k_{g1} - \mu\omega_g$ . If we use the normalization in Eq. (15) the equations above can be written as (for square cells)

$$(1 - v_0^2)\hat{k}_1^2 + \hat{k}_2^2 - 2\beta\hat{\xi}\hat{k}_1 - \hat{\xi}^2 = 0 \quad (25)$$

where  $\hat{\xi} = \beta\nu_1 - \mu\lambda_1$ . The positions of the unstable NCI modes in  $\hat{\mathbf{k}}$  space depends only on  $\Delta t$  and  $\Delta x_i$  through their ratio  $\lambda_1$ . Therefore, the position of the  $|\nu_1| \geq 1$  NCI does not change if one keeps the ratio of time step to cell size. Moreover, if  $\mu = 0$ ,  $\lambda_1$  does not appear in Eq. (25), which means that the position of the  $(\mu, \nu_1) = (0, \pm 1)$  modes are not affected by the time step at all (except for the very minor change since  $[\omega] \rightarrow \omega$  when time step is reduced).

For the NCI at  $(\mu, \nu_1) = (0, 0)$ , there is no intersection between the corresponding fundamental Langmuir mode and the EM mode [as can be seen by plotting Eq. (12) and (13) in  $(\omega, k_1)$  space, see Fig. 3 (a)]. The two modes

interact at highly localized positions determined by the coupling term in Eq. (9). To show how the coupling term in Eq. (9) modifies the Langmuir and EM modes, we plot the solution of Eq. (9) at  $\hat{k}_1 \approx 0.21$ ,  $-0.07 \leq \hat{k}_2 \leq -0.02$ , where the instability is observed. Equation (9) is solved both with, and without the coupling term (numerically forcing the coupling term to be zero). The parameters used in solving Eq. (9) numerically are the same as in Table 1, with  $(\mu, \nu_1) = (0, 0)$ . It is evident in Fig. 3 (a) and (c) that when the coupling term is present, the fundamental Langmuir mode and EM mode are coupled near  $-0.057 \leq \hat{k}_2 \leq -0.037$ . In Fig. 3 (c) where the growth rate is plotted, it becomes clear that in this range of  $k_2$  where the fundamental Langmuir mode and EM mode are coupled, the two modes become complex conjugate pairs with one of them corresponding to instability in this range of  $k_2$ . In Figs. 3 (b) and (d), we scan ranges in both  $k_1$  and  $k_2$ , specifically, we scan the range  $\hat{k}_1 \in [-0.28, -0.15]$  and  $\hat{k}_2 \in [-0.07, -0.02]$ .

We next investigate the sensitivity of the growth rate and location in  $\mathbf{k}$ -space to the simulation parameters for the NCI at the fundamental mode  $(\mu, \nu_1) = (0, 0)$ . Note that we define the position of these modes at the value of  $(\hat{k}_1, \hat{k}_2)$  where the growth rate is maximum. In reality there is a range (although highly localized) of modes that go unstable. Fig. 4 (a)–(d) shows how the positions and growth rates of those modes change with plasma density and time step. For each simulation setup we plot both the simulation results and the predictions from the analytical expressions. When changing the grid sizes we fix  $\Delta x_1 = \Delta x_2$ . Fig. 4 (a) shows that when the grid sizes increases, the position of the  $(\mu, \nu_1) = (0, 0)$  NCI moves farther away from the center of the  $(k_1, k_2)$  plot where the interesting real physics resides [red curve in Fig. 4 (a)]. We keep  $\Delta t$  constant as  $\Delta x_1$  changes. This mode also moves farther away from the interesting physics when the time step decreases [see red curve in Fig. 4 (b)]. Furthermore, as shown in Fig. 4 (c), the growth rate decreases as the time step decreases [blue curve], which is not the case for the fastest growing modes of the NCI. The growth rate also decreases when the grid size increases while keeping  $\Delta t$  fixed [Fig. 4 (c) red curve]. When the density of the plasma increases (while fixing  $\gamma_b = 50$ ), the position of the  $(\mu, \nu_1) = (0, 0)$  NCI moves away from the center in  $(k_1, k_2)$  space, and the growth rate of the unstable modes increases [Fig. 4 (d)].

A parameter scan which shows how the growth rate and position of the most unstable  $(\mu, \nu_1) = (0, 0)$  modes change with different choices of the grid sizes and time step, is shown in Fig. 5. Note that we are keeping  $\Delta x_1 = \Delta x_2$  in the parameter scan. By examining Fig. 5, we see that



by reducing the  $\Delta t/\Delta x_1$  ratio, the instability at the fundamental Langmuir mode moves farther towards larger  $\hat{k}_1$  and the growth rate decreases. This indicates when the grid size is restricted to resolve the characteristic length of physical modes, the position of the  $(\mu, \nu_1) = (0, 0)$  mode can be moved to larger  $\hat{k}_1$  by simply using a smaller time step.

Meanwhile, when the time step is fixed, the growth rates of higher order NCI ( $|\nu_1| > 1$ ) unstable modes can be efficiently reduced by using higher order particle shapes. In Fig. 6 (a) we show how using different particle shapes changes the growth rate of the various NCI modes. We used the parameters in Table 1 for this figure. The result indicates that, while using higher order particle shapes is very efficient in reducing the growth rate of higher order NCI modes, it is less efficient for the  $(\mu, \nu_1) = (0, 0)$  mode. We also compared results with different grid sizes (while fixing  $\Delta t/\Delta x_1 = 0.4$ ), as shown in Fig. 6 (b). It indicates that reducing the grid size (while fixing  $\Delta t/\Delta x_1$ ) helps reduce the growth rate of the  $(\mu, \nu_1) = (0, 0)$  mode, but not for the modes with  $\nu_1 \neq 0$ .

### 3. Strategies for eliminating NCI and sample simulations

Based on this new understanding of the behavior of the unstable NCI modes, we now discuss approaches for controlling it. Once the NCI is adequately controlled, high fidelity simulations of relativistically drifting plasma can be carried out. We concentrate on spectral solvers and note that others are developing approaches for finite difference solvers [15]. The new form for the dispersion relation in Eq. (9) can also be used to investigate the NCI for other solvers and we leave this for future work.

The approach we use is to first move the unstable modes to large  $\hat{\mathbf{k}}$ 's that are outside the region  $\hat{\mathbf{k}}$  where important physics is occurring. As discussed in [12], for the spectral solver the fastest growing modes at  $(\mu, \nu_1) = (0, \pm 1)$  exist at large  $|\hat{\mathbf{k}}|$  (the edge of the fundamental Brillouin zone), and as discussed earlier in section 2 their location in  $\hat{\mathbf{k}}$ -space does not change much as the grid size and time step are varied.

As discussed earlier in section 2 and shown in Fig. 2, the second fastest growing mode at  $(\mu, \nu_1) = (0, 0)$  is localized in  $\hat{\mathbf{k}}$ -space and can be removed through a mask (filter). However, these modes may exist near modes of physical interest, and for LWFA boosted frame simulations the plasma only exists in a small region of the simulation window. For such situations simply applying a mask filter may also effect the physics. We therefore eliminate

those modes by reducing the time step (while keeping the cell size fixed). As shown in Figs. 5 (a) and (b), this both moves the unstable modes to higher  $k_1$  and lowers the growth rate. Once the modes are outside the range of physical modes a filter (mask) can be applied if necessary.

To investigate how reducing the time step changes the NCI, 2D simulations using the same parameters as the one shown in Fig. 2, but with a reduced time step of  $\Delta t = 0.1\Delta x_1$  are conducted. The corresponding beam resonances for this time step are illustrated in Fig. 7 (a), while the corresponding simulation data and analytical prediction for  $\Delta t = 0.1\Delta x_1$  are shown in Fig. 7 (c)–(f). From Fig. 7 (c) and (e) we see as expected that when the time step is reduced, the growth rate and pattern of the fastest growing modes at  $(\mu, \nu_1) = (0, \pm 1)$  do not change much [compared with Fig. 2 (a) and (b)]. However, for the  $(\mu, \nu_1) = (0, 0)$  modes shown in Fig. 7 (d) and (f), the locations move away from the center [compared with Fig. 2 (c) and (d)], while the growth rate is reduced by approximately a factor of 4.

In addition, when the time step is reduced to suppress the  $(\mu, \nu_1) = (0, 0)$  mode, the locations and growth rate for the higher order  $|\nu_1| > 1$  modes also change. As seen in Fig. 7 (a), the next beam resonance after  $(\mu, \nu_1) = (0, \pm 1)$  is  $(\mu, \nu_1) = (0, \pm 2)$  rather than  $(\mu, \nu_1) = (1, \pm 1)$ . It is easy to see that in this case the  $(\mu, \nu_1) = (0, \pm 2)$  resonance line has no intersection with the EM mode in the fundamental Brillouin zone. The beam resonance line for an intermediate time step of  $\Delta t = 0.225\Delta x_1$  are likewise shown in Fig. 7 (b). They show how gradually reducing the time step changes the NCI modes in the fundamental zone.

In the following, we will use these approaches to essentially eliminate the NCI in LWFA simulations in a Lorentz boosted frame, and in relativistic collisionless shock simulation, both of which involves the modeling of relativistically drifting plasma.

### *3.1. LWFA simulation in the Lorentz boosted frame*

We next present results from an LWFA boosted frame simulations in a nonlinear regime which is much more challenging. As shown in Ref. [13] excellent agreement between lab frame and boosted frame simulations are obtained in the linear regime using UPIC-EMMA when the fastest growing mode is filtered out. For simulation of nonlinear cases slight differences appear at higher  $\gamma_b$ . We revisit these simulations using strategies to systematically suppress the NCI modes.

Before we present the results, we note that in LWFA simulations the plasma density is not really a free parameter when the simulation is done in the  $\gamma_w$  frame where  $\gamma_w \equiv \omega_0/\omega_{p0}$ ,  $\omega_0$  is the laser frequency. In this frame  $\omega' = \gamma_b(\omega_0 - k_0 v_b) = 2\omega_0/\gamma_b$ , and  $\omega_p^2/\gamma$  is an invariant,  $\omega_p^2/\gamma = \omega_{p0}^2$ , which leads to

$$\frac{\omega_p^2}{\gamma\omega'^2} = \frac{\omega_{p0}^2\gamma^2}{4\omega_0^2} = \frac{1}{4} \quad (26)$$

Therefore, with respect to  $\omega'$  the value of  $\omega_p^2/\gamma$  is fixed. The time steps and cell sizes are determined with respect to  $\omega'$ , therefore  $\omega_p^2/\gamma$  is not a free parameter.

In Fig. 8 we present results from a 2D LWFA simulations in the Lorentz boosted frame. The simulation parameters are the same as in Ref. [13] with  $\gamma_b = 28$ . The time step used in [13] is  $\Delta t = 0.221\Delta x_1$ , which is about 1/2 of the 2D Courant limit for a standard spectral solver, and we used  $\Delta t = 0.0525\Delta x_1$ , which is about 1/8 the Courant limit in the new cases. In Ref. [13], for the case with  $\gamma_b = 28$  we observed self-trapped particles that leads to a slightly different wake, as compared with both the  $\gamma_b = 14$  case and the lab frame simulation. In Fig. 8 (c) and (d) we show that by simply reducing the time step, we obtain results that are closer to the lab frame simulation. The plots of  $E_2$  and plasma density also show subtle differences. The self-trapped electrons located at  $k_0 x_1 = 3.2 \times 10^4$  in the upper row of Fig. 8 are absent in the middle row. Note in the 2D OSIRIS lab frame simulation no self-trapped particles are observed. A consistent interpretation is also seen when transforming the boosted frame data back to the lab frame. In Fig. 8 (e) we plot the line out of the  $E_1$  wake field. This plot is the same as the second row of Fig. 8 in Ref. [13], except for the added data with  $\Delta t = 0.0525\Delta x_1$  (black curves). It shows that better agreement to the lab frame and  $\gamma_b = 14$  cases are found for the  $\gamma_b = 28$  when the reduced time step are used (no self-trapped particles are seen in the lab frame and  $\gamma_b = 14$  cases). For the simulation parameters of the reference simulation, the  $(\mu, \nu_1) = (0, 0)$  mode is localized near  $(\hat{k}_1, \hat{k}_2) = (0.24, 0.037)$  and the growth rate is  $0.0341\omega_p$ . For the reduced time step of  $\Delta t/\Delta x_1 = 0.0525$ , the  $(\mu, \nu_1) = (0, 0)$  modes move to  $(\hat{k}_1, \hat{k}_2) = (0.41, 0.023)$  and the growth rate is reduced to  $0.0092\omega_p$ .

Parameters	Values
grid size ( $\Delta x_1, \Delta x_2$ )	$(0.5k_0^{-1}, 0.5k_0^{-1})$
time step $\Delta t$	$0.4\Delta x_1, 0.08\Delta x_1$
number of grid	$32768 \times 512$
particle shape	quadratic
Drifting gamma	$\gamma = 20.0$

Table 2: Simulation parameters for the 2D shock simulation.  $n_p$  is the reference plasma density, and  $\omega_p^2 = 4\pi q^2 n_p / m_e$ ,  $k_p = \omega_p$  ( $c$  is normalized to 1).

### 3.2. Relativistic collisionless shock

In Fig. 9 we present the results of two colliding plasma simulations, using the parameters in Table 2, with two different time steps. In these simulations we model the interaction of two counter-streaming plasma flows, each moving with a relativistic Lorentz factor of 20.0. As the two flows interpenetrate they give rise to the Weibel instability, which slows down the flows and forms two shocks that propagate in opposite directions. In both cases we use the low-pass filter to eliminate the  $\nu_1 = \pm 1$  NCI. Comparing Fig. 9 (b) with  $\Delta t = 0.4\Delta x_1$  and (c) with  $\Delta t = 0.08\Delta x_1$ , it is evident that when the time step is reduced, the noise originating from the NCI in the region of the two streams that have not yet collided (overlap) with their counter stream is much smaller (note in 2D, NCI is evident in  $E_2$  and  $B_3$ ). The plasma density for the smaller time step at the same physical time is shown in Fig. 9 (a) to show the parts of the two streams that have not overlapped yet.

## 4. 3D Scenario

We next discuss the NCI in three dimensions. Based on the results for the 2D case, we write the full dispersion relation into the coupling between a Langmuir and an EM mode. For the spectral solver, the dispersion relation

for a specific  $\mu$ ,  $\nu_1$  mode can be rewritten as,

$$\begin{aligned} & \left( [\omega]^2 - k_1^2 - k_2^2 - k_3^2 - \frac{\omega_p^2}{\gamma} (-1)^\mu S_j \frac{S_E[\omega] - S_B k_1 v_0}{\omega' - k_1' v_0} \right) \\ & \left\{ \left( (\omega' - k_1' v_0)^2 - \frac{\omega_p^2}{\gamma^3} (-1)^\mu \frac{S_j S_E \omega'}{[\omega]} \right) \left( [\omega]^2 - k_1^2 - k_2^2 - k_3^2 - \frac{\omega_p^2}{\gamma} (-1)^\mu S_j \frac{S_E[\omega] - S_B k_1 v_0}{\omega' - k_1' v_0} \right) \right. \\ & \left. + \frac{\omega_p^2}{\gamma [\omega]} (-1)^\mu S_j (k_2^2 + k_3^2) \{v_0^2 (S_E \omega - S_B [\omega]) - v_0 \nu_1 S_E k_{g1}\} \right\} = 0 \end{aligned} \quad (27)$$

For the instability mode near the resonance line, we can assume

$$\left( [\omega]^2 - k_1^2 - k_2^2 - k_3^2 - \frac{\omega_p^2}{\gamma} (-1)^\mu S_j \frac{S_E[\omega] - S_B k_1 v_0}{\omega' - k_1' v_0} \right) \neq 0 \quad (28)$$

$$\begin{aligned} & \left( (\omega' - k_1' v_0)^2 - \frac{\omega_p^2}{\gamma^3} (-1)^\mu \frac{S_j S_E \omega'}{[\omega]} \right) \left( [\omega]^2 - k_1^2 - k_2^2 - k_3^2 - \frac{\omega_p^2}{\gamma} (-1)^\mu S_j \frac{S_E[\omega] - S_B k_1 v_0}{\omega' - k_1' v_0} \right) \\ & + \frac{\omega_p^2}{\gamma [\omega]} (-1)^\mu S_j (k_2^2 + k_3^2) \{v_0^2 (S_E \omega - S_B [\omega]) - v_0 \nu_1 S_E k_{g1}\} = 0 \end{aligned} \quad (29)$$

which, as in the 2D case, can be viewed as the coupling between the Langmuir and EM mode. When Eq. (29) is compared with Eq. (22), we can see the equations in 3D can be obtained by replacing  $k_2^2$  with  $k_2^2 + k_3^2$  in its 2D counterpart. As a result, the pattern of instability in 3D can be conveniently deduced. The location of the  $(\mu, \nu_1) = (0, 0)$  NCI modes in  $\mathbf{k}$  space in 3D can be obtained as follows. Pick a point in  $(k_2, k_3)$  space, then the growth rate and location in  $k_1$  space of this mode will be the same as for  $k_2^{2D} = \sqrt{k_2^{2D} + k_3^{3D}}$ , where  $k_{1,2,3}^{3D}$  and  $k_{1,2}^{2D}$  are the coordinates of the NCI modes in the 3D and 2D scenario respectively (assuming  $\Delta x_1^{3D} = \Delta x_2^{3D} = \Delta x_3^{3D} = \Delta x_1^{2D} = \Delta x_2^{2D}$  and  $\Delta t^{3D} = \Delta t^{2D}$ ). This indicates that the unstable modes form “ring” pattern in the  $(k_2, k_3)$  space at specific values of  $\hat{k}_1$ . In addition, the maximum growth rate  $\tau$  of these modes has  $\tau^{2D} \approx \tau^{3D}$  when  $\Delta x_1^{3D} = \Delta x_2^{3D} = \Delta x_3^{3D} = \Delta x_1^{2D} = \Delta x_2^{2D}$  and  $\Delta t^{3D} = \Delta t^{2D}$ .

In Fig. 10 we present data from a 3D simulation of a drifting plasma, using the same parameters as in Table 1 except now  $\Delta t^{3D} = 0.35 \Delta x_1$  (so that the Courant condition is satisfied). The different values of  $\Delta t$  and the different noise sources in 3D v.s. 2D means the results will not be identical. We plot the FFT of  $E_2$  in each panel. In Fig. 10 (a) the real frequency v.s.  $\hat{k}_1$  are plotted along with the line  $\hat{\omega}_r = \hat{k}_1 \beta$ . This data was obtained for a line out along  $x_1$  located at the middle of the box. In Fig. 10 (b) a 3D plot

of  $E_2$  in  $\mathbf{k}$ -space is shown at a time during the exponential growth (before saturation). Only modes with amplitudes above 1/30 of the maximum mode are plotted. The predicted rings are clearly present. In Fig. 10 (c) and (d) cross sections of the plot in Fig. 10 (b) are shown.

In analogy with the 2D case, we can filter out this instability by applying a mask filter to eliminate the corresponding modes in the ring. For example we have a mask that blocks out all the modes between

$$0.175 \leq \hat{k}_1 \leq 0.275 \quad 0.027^2 \leq \hat{k}_2^2 + \hat{k}_3^2 \leq 0.067^2$$

A parameter scan of the growth rate and position of the unstable modes using UPIC-EMMA, as well as comparison between the analytical predictions is presented in Fig. 11 (a)–(d). The variable  $k_R$  in these plots refers to the radius of the ring pattern. It confirms that when comparing the unstable mode for a 2D case (see Fig. 4) against its counterpart in 3D, we have approximately  $\hat{k}_1^{3D} = \hat{k}_1^{2D}$ , and  $\hat{k}_R^2 \equiv (\hat{k}_2^{3D})^2 + (\hat{k}_3^{3D})^2 = (\hat{k}_2^{2D})^2$  (where  $\hat{k}_R = k_R/k_{g1}$ ), and  $\tau^{3D} \approx \tau^{2D}$ . Therefore, the 3D NCI can effectively be eliminated by using the same strategies as in 2D.

As example of a three dimensional case, we revisit the 3D LWFA boosted frame simulation presented in Ref. [13] using a time step of  $\Delta t = 0.2\Delta x_1$ . Results are shown in Fig. 12. This simulation uses a low-pass filter to eliminate the  $(0, \pm 1)$  mode. The simulation was rerun with the reduced time step of  $\Delta t = 0.0667\Delta x_1$  to ensure elimination of the  $(0, 0)$  modes while a low-pass filter is used to eliminate the  $(0, \pm 1)$  mode. Other parameters for these two simulations are listed in Table 2 of Ref. [13]. As seen in Fig. 12, the plasma density are similar for the two time steps of the two boosted frame cases, although there are subtle differences. In Fig. 12 (c), data is transformed back to the lab frame and a line out of the  $E_1$  is plotted. There is general agreement between all three cases. Nonetheless, it is interesting to note that there are differences. As seen in Fig. 12 (c) the  $\Delta t = 0.0667\Delta x_1$  case (red curve) shows slightly heavier beam loading in the first bucket than in the  $\Delta t = 0.2\Delta x_1$  case (green curve), and both boosted frame cases show more beam loading than in the lab frame case (blue curve). There are also differences in the later buckets. This result, and the 2D results discussed in section 3.1 reveals the fact that the modeling nonlinear wakes and the self-injection process much more challenging than linear or weakly nonlinear wake fields where there is much better agreement. This result also shows that in any given simulation it is not obvious if the higher order NCI modes

are an issue. However, as alluded to earlier, the spectral (FFT based) solvers have the advantage that the accuracy of the simulation for given cell sizes and number of particles per cell improve as the time step is reduced. This occurs because the NCI modes are less of an issue and the overall accuracy of the particle push and numerical dispersion also improve.

## 5. Summary

We have systematically investigate the unstable NCI modes with an emphasis for a spectral (FFT) based Maxwell solver. We start from a general dispersion relation described in previous work [12]. This previous work and that of others shows that the unstable NCI modes occur near the intersection of wave particle resonances (including aliases), i.e., where  $\omega' - k'_1\beta = 0$ , and electromagnetic waves. Therefore, each unstable mode can be identified as coming from a specific value of  $\mu$  and  $\nu_1$ . Based on this information, we rewrite the dispersion relation in both 2D and 3D for given values of  $\mu$  and  $\nu_1$  into the coupling between two modes which are each numerically stable, and for which the coupling term vanishes in the continuous limit. These two modes are easily identified as the Lorentz transformed version of modes which are purely longitudinal (Langmuir) and purely transverse (EM) in the rest frame of the plasma. We then use the new form of the NCI dispersion relation to study the NCI for a spectral (FFT) based Maxwell solver. The fastest growing modes corresponding to  $(\mu, \nu_1) = (0, \pm 1)$  were studied in Ref. [12] and [13]. Here, we studied additional modes with  $(\mu, \nu_1) = (0, 0)$  and  $|\nu_1| > 1$ . We find for the FFT solver that the second fastest growing mode is at  $(\mu, \nu_1) = (0, 0)$  and that unlike the  $(\mu, \nu_1) = (0, \pm 1)$  mode its location moves to larger values of  $\hat{k}_1$  and its growth rate goes to zero as  $\Delta t/\Delta x \rightarrow 0$ .

Unlike the NCI modes with  $|\nu_1| > 0$ , the NCI at the fundamental Langmuir resonance has a highly localized pattern of four dots in the  $\mathbf{k}$  space in 2D (one in each quadrant); while in 3D the unstable modes form a ring pattern. A simple relation of the growth rate and locations of this instability between the 2D scenario and 3D scenario is found with  $\hat{k}_1^{3D} = \hat{k}_1^{2D}$ , and  $(\hat{k}_2^{3D})^2 + (\hat{k}_3^{3D})^2 = (\hat{k}_2^{2D})^2$ , and  $\tau^{2D} \approx \tau^{3D}$  when  $\Delta x_1^{3D} = \Delta x_2^{3D} = \Delta x_3^{3D} = \Delta x_1^{2D} = \Delta x_2^{2D}$  and  $\Delta t^{3D} = \Delta t^{2D}$  is assumed.

Based on the new understanding of the family of unstable NCI modes, we developed strategies for eliminating them with an emphasis for a spectral solver. The principle idea is to ensure the unstable modes are far away from the physics of interest. Note that according to Eq. (25) the  $\nu_1 = \pm 1$  NCI

always resides far away from the interested physics. The  $\nu_1 = 0$  mode can be moved away towards large  $\hat{\mathbf{k}}_1$  by reducing the time step. A dedicated mask filter can then be applied in the solver to eliminate these modes without affecting the modes of physical interest. Since the growth rate of the  $\nu_1 = 0$  NCI decreases as the time step is decreased, in some cases it is not necessary to apply the mask filter to eliminate this mode. Furthermore, the growth rates of the higher order NCI modes with  $|\nu_1| > 1$  are reduced when using higher order particle shapes and they are also modified as the time step is reduced. We have used these strategies in UPIC-EMMA simulations of both LWFA simulation in a Lorentz boosted frame and of colliding plasmas (as is done when simulating relativistic collisionless shocks). In both cases the results show that the NCI is effectively eliminated when a low pass filter is used to eliminate the  $(\mu, \nu_1) = (0, \pm 1)$  mode and the time step is reduced for suppressing the  $(\mu, \nu_1) = (0, 0)$  and  $|\nu_1| > 1$  modes.

For future work we will investigate the tradeoff between the two mitigation strategies discussed in this paper. Currently, we reduce the time step to eliminate possible spurious effects associated with the  $(0,0)$  mode. However, when doing a physics simulation signals at all values of  $\hat{\mathbf{k}}$  occur. So determining *a priori* what time step can be used is not possible. However, one advantage of the spectral solver is the accuracy of all the physics improves as the time step is reduced (this is not true for finite difference solvers as this can lead to large dispersion errors in EM waves). So once a time step is found for which the results have converged, one can investigate how the results compare with a combination of a mask filter and intermediate time step. In addition, since the plasma only exists in a finite region of the box, the filter should only be applied in that spatial domain. Developing methods to do this might improve the results. Furthermore, studying how the physics changes as the time step is reduced and how results actually converge is also an important area for future work. Another area for future work is to develop filters and interpolation schemes that cancel the coupling term,  $\mathcal{C}$ . This approach would have overlap with the finite difference solver investigations [15].

This work was supported by US DOE under grants DE-SC0008491, DE-SC0008316, DE-FC02-04ER54789, DE-FG02-92ER40727, by the US National Science Foundation under the grant ACI 1339893, and by NSFC Grant 11175102, thousand young talents program, and by FCT (Portugal), grant EXPL/FIS-PLA/0834/1012, and by the European Research Council (ERC-2010-AdG Grant 267841), and by LLNL's Lawrence Fellowship. Simulations



were carried out on the UCLA Hoffman2 and Dawson2 Clusters, and on Hopper cluster of the National Energy Research Scientific Computing Center.

## References

- [1] J. -L. Vay, Phys. Rev. Lett. 98, 130405 (2007)
- [2] S. F. Martins, R. A. Fonseca, W. Lu, W. B. Mori and L. O. Silva, Nat. Phys. Vol. 6, 311 (2010)
- [3] J.-L. Vay, C.G.R. Geddes, E. Esarey, C.B. Schroeder, W.P. Leemans, Phys. Plasmas 18 (2011) 123103.
- [4] S. F. Martins, R. A. Fonseca, L. O. Silva, W. Lu, W. B. Mori, Comp. Phys. Comm. 181, 869 (2010)
- [5] S. F. Martins, R. A. Fonseca, W. B. Mori, L. O. Silva, Astrophys. J. Lett. 695, L189–L193 (2009).
- [6] F. Fiuza, R. A. Fonseca, J. Tonge, W. B. Mori, and L. O. Silva, Phys. Rev. Lett., 108, 235004 (2012).
- [7] B. B. Godfrey, J. Comp. Phys. 15, 504 (1974)
- [8] B. B. Godfrey, J. Comp. Phys. 19, 58 (1975)
- [9] J. -L. Vay, C. G. R. Geddes, E. Cormier-Michel, D. P. Grote, J. Comp. Phys. 230, 5908 (2011).
- [10] P. Yu et.al, in Proc. 15th Advanced Accelerator Concepts Workshop, Austin, TX, 2012.
- [11] B. B. Godfrey and J.-L. Vay, J. Comp. Phys., 248, 33-46 (2013)
- [12] X. Xu, et. al., Comp. Phys. Comm., Vol. 184, 2503–2514 (2013)
- [13] P. Yu, et. al., J. Comp. Phys. 266, 124 (2014)
- [14] B. B. Godfrey, J.-L. Vay, I. Haber, J. Comp. Phys. 258, 689 (2014)
- [15] B. B. Godfrey, J. -L. Vay, J. Comp. Phys. 267, 1 (2014)

- [16] E. L. Lindman, *J. Comp. Phys.* 5, 13 (1970); A. B. Langdon, *J. Comp. Phys.* 6, 247 (1970).
- [17] C. K. Birdsall, A. B. Langdon, *Plasma Physics via Computer Simulation*, McGraw Hill, New York, 1985.
- [18] J. M. Dawson, *Rev. Modern Phys.*, Vol. 55, No. 2, 403 (1983)
- [19] A. T. Lin, J. M. Dawson, H. Okuda, *Phys. Fluids*, Vol. 17, 1995 (1974).
- [20] K. Yee, *IEEE Transactions on Antennas and Propagation*, Vol. 14, 302 (1966)
- [21] M. Karkkainen, E. Gjonaj, T. Lau, T. Weiland, in *Proc. International Computational Accelerator Physics Conference*, Chamonix, France, 2006, pp. 35–40.

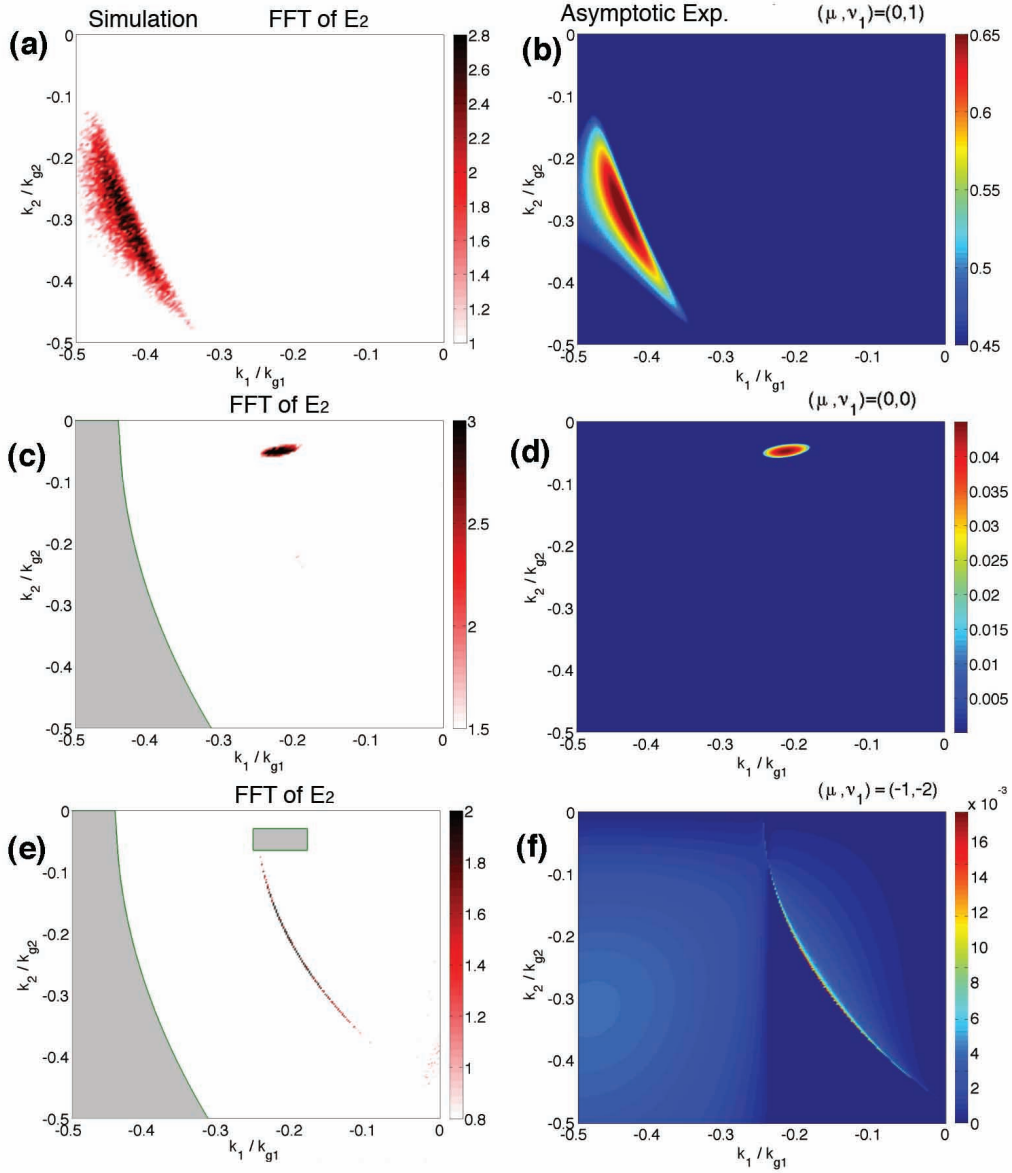


Figure 2: (a), (c), and (e) are the FFT of  $E_2$  in the 2D simulations using the parameters listed in Table 1. The filter applied in order to observe these modes are illustrated by the grey areas in the plots. (b), (d), and (f) are the corresponding predictions by using the expression Eq. (18) and (23).

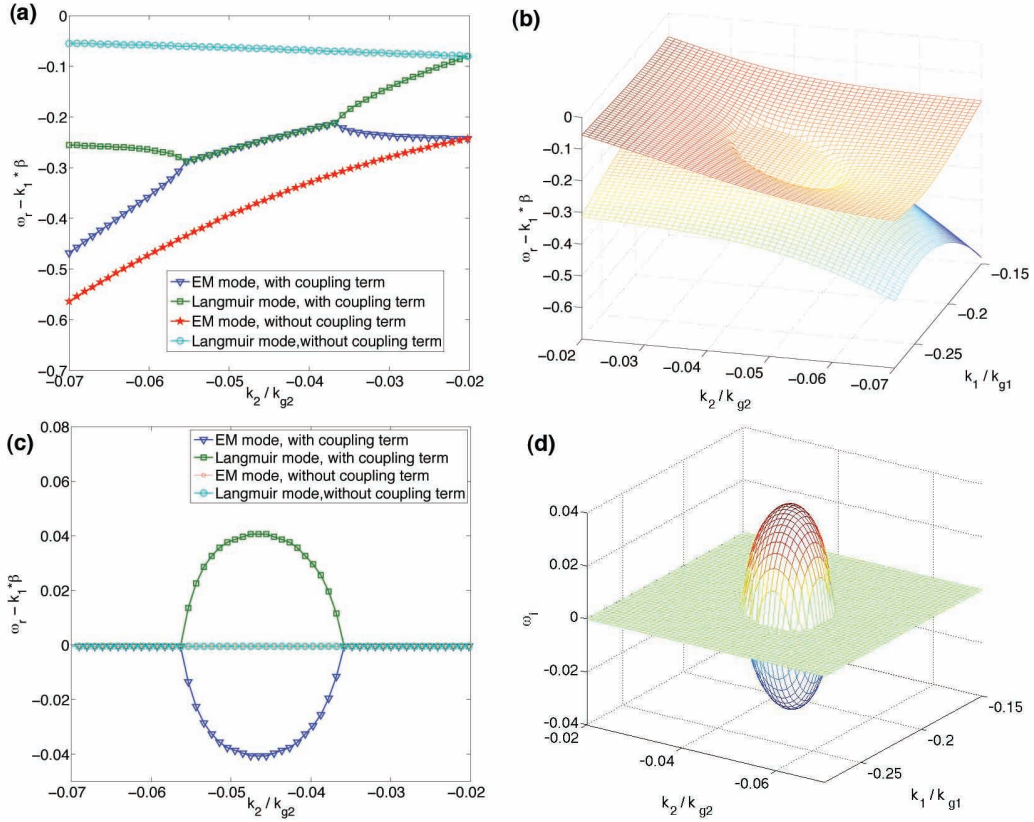


Figure 3: Roots of Eq. (9) under the parameters listed in Table 1. (a) and (c) shows the real, and imaginary parts of the roots between  $\hat{k}_1 = 0.21$ , and  $-0.07 \leq \hat{k}_2 \leq -0.2$ , both with and without the coupling terms; meanwhile (b) and (d) shows the real and imaginary part of the roots in the range  $-0.28 \leq \hat{k}_1 \leq -0.15$  and  $-0.07 \leq \hat{k}_2 \leq -0.02$ .

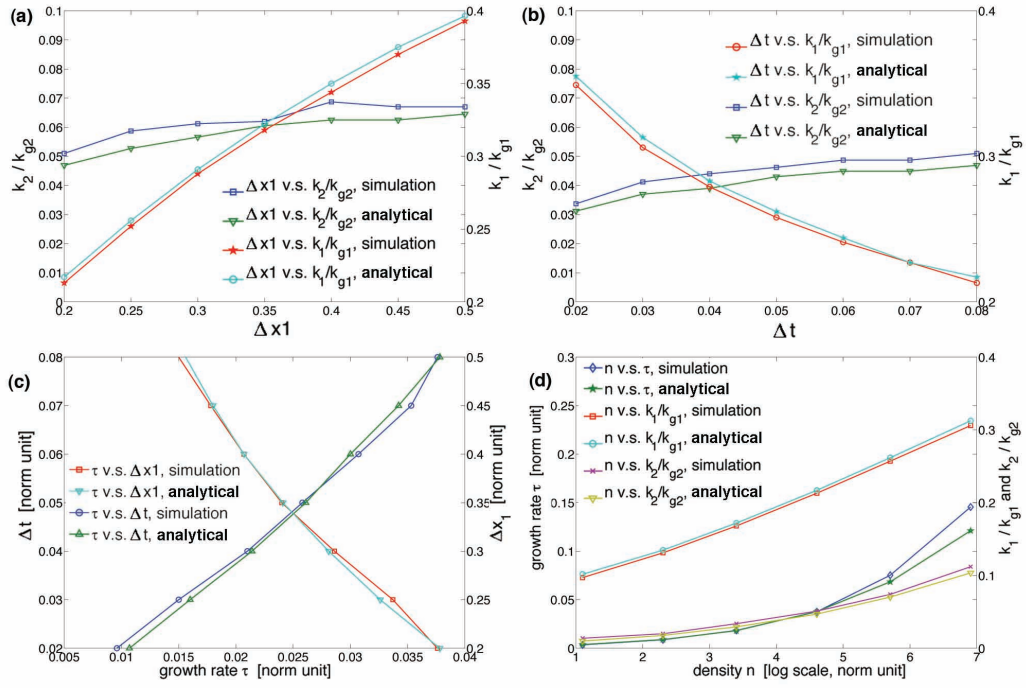


Figure 4: Dependence of the position  $(\hat{k}_1, \hat{k}_2)$ , as well as the growth rate  $\tau$  of the NCI at the fundamental Langmuir mode to grid sizes  $\Delta x_1$  (with  $\Delta x_1 = \Delta x_2$  fixed), time step  $\Delta t$ , and plasma density  $n_0$ .

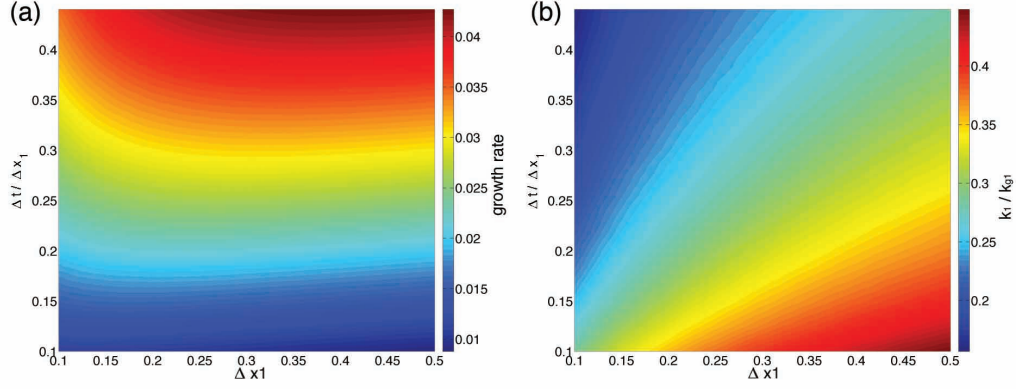


Figure 5: Dependence of the (a) growth rate, and (b)  $k_1$  position of NCI at the fundamental Langmuir mode for grid sizes  $0.1 \leq \Delta x_1 \leq 0.5$  (with  $\Delta x_1 = \Delta x_2$  fixed), and  $0.1 \leq \Delta t / \Delta x_1 \leq 0.45$ .

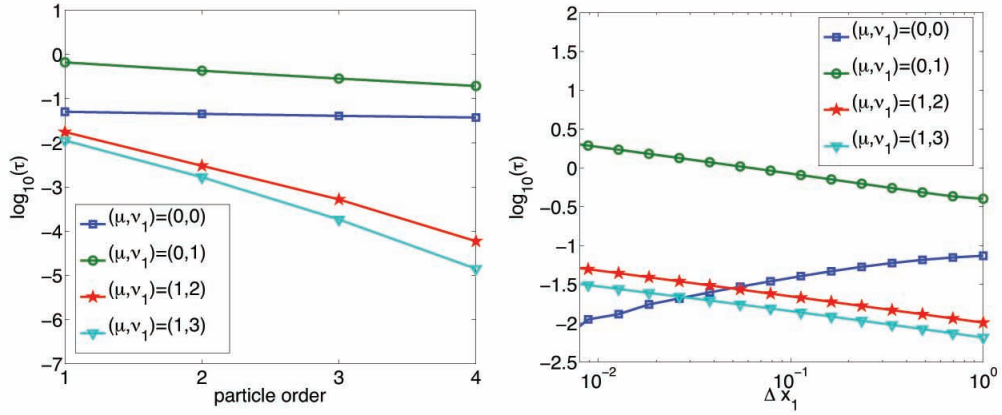


Figure 6: (a) shows the dependence of the growth rate on grid size for various  $\nu_1$  modes; (b) shows the dependence of the growth rate  $\tau$  on particle shapes. Parameters listed in Table 1 are used for these plots.

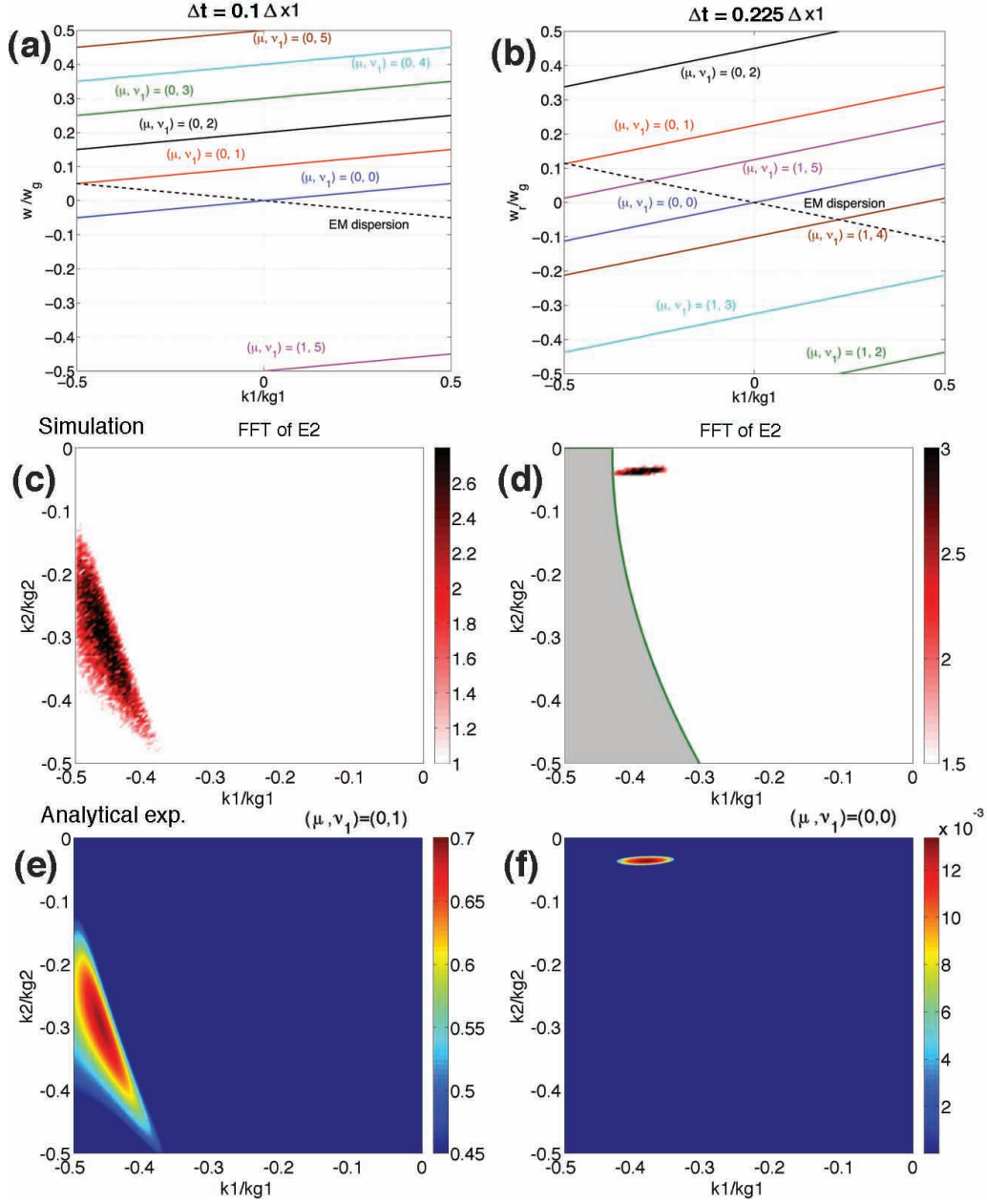


Figure 7: (a) and (b) show the EM dispersion relation together with the beam resonance  $\omega' - k_1' \beta = 0$ , for  $\Delta t = 0.1 \Delta x_1$  and  $\Delta t = 0.225 \Delta x_1$  (and other parameters the same as listed in Table 1). (c) and (d) are the FFT of  $E_2$  in the corresponding 2D simulations. The filter applied in order to observe the  $(\mu, \nu_1) = (0, 0)$  mode is illustrated by the grey areas in (d). (e) and (f) are the corresponding analytical predictions by using the expression Eq. (18) and (23).

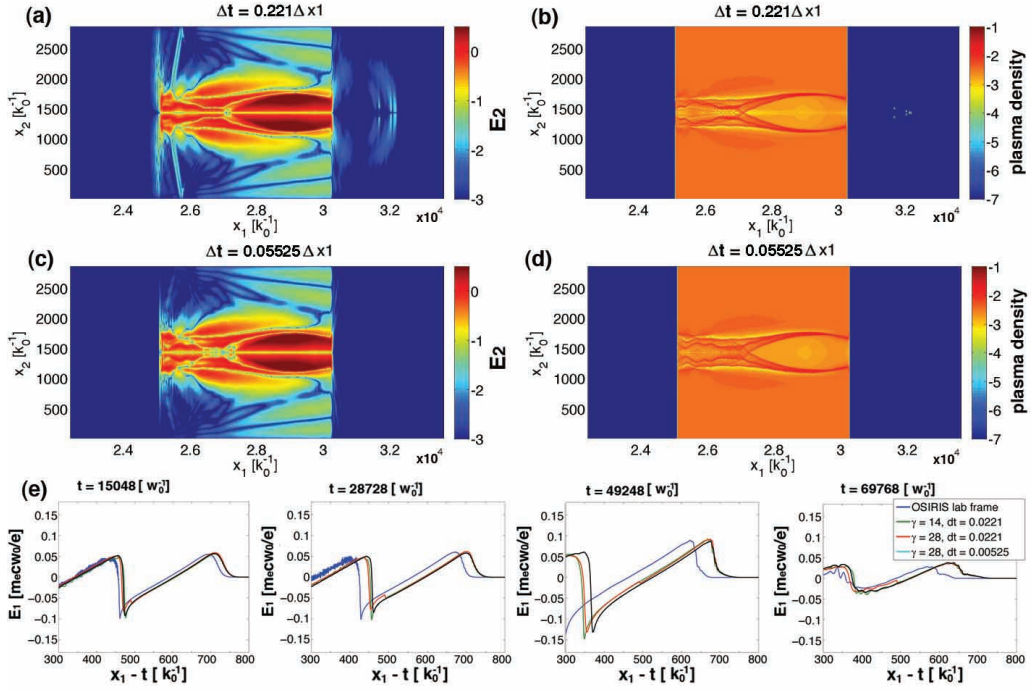


Figure 8: (a) and (c) shows the  $\log_{10}|E_2|$  for the case  $\Delta t = 0.221\Delta x_1$  and  $\Delta t = 0.0525\Delta x_1$ , respectively. (b) and (d) shows the plasma density  $\log_{10}|n|$  for the case  $\Delta t = 0.221\Delta x_1$  and  $\Delta t = 0.0525\Delta x_1$ , respectively. (e) shows the  $E_1$  data comparison of the OSIRIS lab frame simulation, and the 3 UPIC-EMMA simulations.



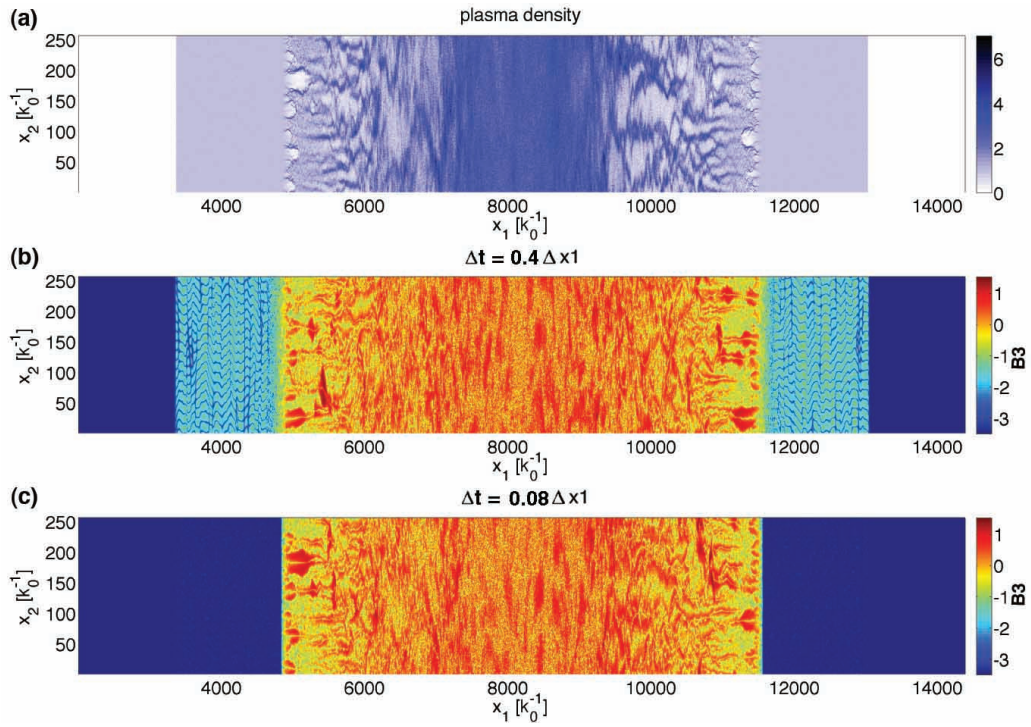


Figure 9: (a) shows the plasma density plot at  $t = 3360 \omega_p^{-1}$  for the  $\Delta t = 0.08\Delta x_1$  case; (b) and (c) show the corresponding  $\log_{10} |B_3|$  for the case  $\Delta t = 0.4\Delta x_1$  and  $\Delta t = 0.08\Delta x_1$ , respectively.

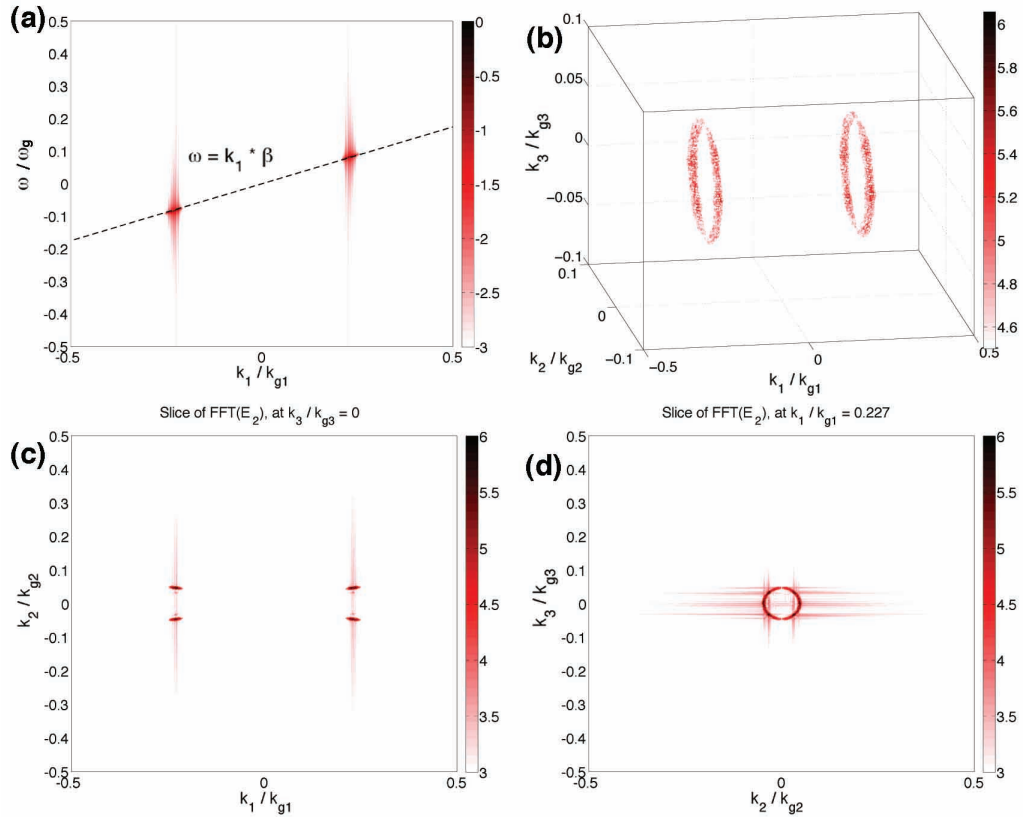


Figure 10: This figure shows the dominant NCI modes after the fastest growing modes are filtered out for a 3D simulation. (a) shows in 3D the  $(\mu, \nu_1) = (0, 0)$  mode which resides at the main resonance  $\omega = k_1 \beta$ ; (b), (c), and (d) are the positions of this NCI mode in  $\hat{\mathbf{k}}$  space.

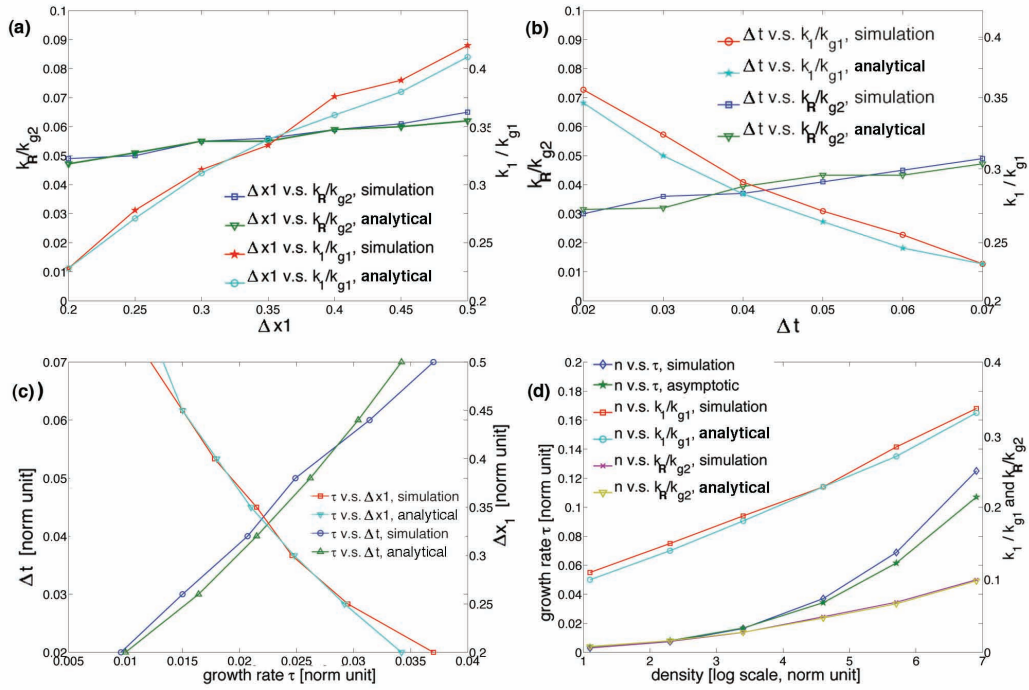


Figure 11: Dependence of the position  $(\hat{k}_1, \hat{k}_2)$ , as well as the growth rate  $\tau$  of the NCI at the fundamental Langmuir mode to grid sizes  $\Delta x_1$  (with  $\Delta x_1 = \Delta x_2$  fixed), time step  $\Delta t$ , and plasma density  $n_0$  in 3D. The variable  $k_R$  refers to the radius of the ring pattern of  $(\mu, \nu_1) = (0, 0)$  NCI modes in 3D.

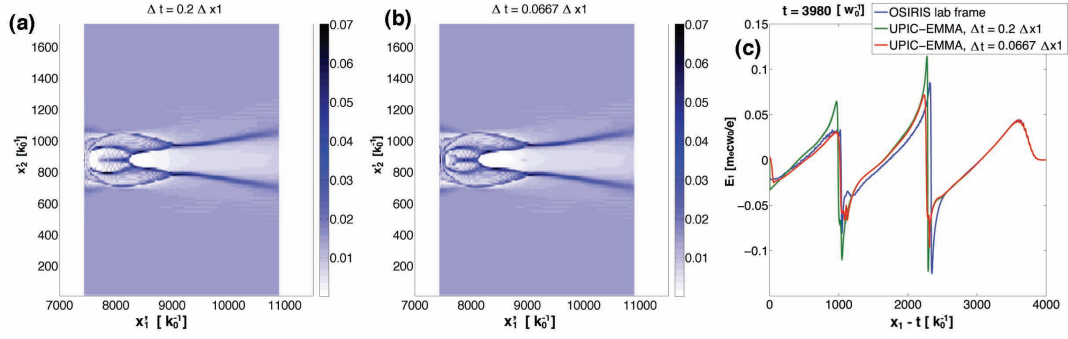


Figure 12: Results from 3D UPIC-EMMA boosted frame simulation ( $\gamma = 17$ ). (a) and (b) present 2D cross section plots of the plasma electron density for  $\Delta t = 0.2\Delta x_1$  and  $\Delta t = 0.0667\Delta x_1$ , while (c) shows the on-axis  $E_1$  comparison between the three cases at  $t = 3980 \omega_0^{-1}$  in the lab frame.  $x_1 - t$  is the coordinates moving together with the moving window.